IAES International Journal of Robotics and Automation (IJRA)
Vol. 15, No. 4, December 2026, pp. 763∼778
ISSN: 2722-2586, DOI: 10.11591/ijra.v15i4.pp763-778

Third-order integral terminal sliding mode control for IPMC soft actuators: design, stability analysis, and multi-frequency simulation study

Dhurgham R. M. Al-Tayar[1], Ali Al-Ghanimi[1], Ibrahim H. Al-Kharsan[1,2]
[1]Department of Electrical Engineering, Faculty of Engineering, University of Kufa, Najaf, Iraq
[2]Department of Electrical Engineering Techniques, College of Technical Engineering, Al-Mustaqbal University, Babylon, Iraq

Article Info

Article history:

Received May 5, 2026
Revised Aug 10, 2026
Accepted Nov 10, 2026

Keywords:

Finite-time convergence
IPMC actuator
Mechatronic systems
Precision positioning
Robust control
Sliding mode control
Soft actuator
Terminal sliding mode

ABSTRACT

This paper reports the first application of continuous third-order integral terminal sliding mode control (3-ITSMC) to an ionic polymer-metal composite (IPMC) soft actuator, targeting high-precision motion tracking in mechatronic positioning systems. The novelty lies in combining an integral terminal sliding surface with a third-order super-twisting algorithm for a strongly uncertain, back-relaxing soft actuator, giving finite-time convergence and chattering-free actuation, while a filtered derivative scheme enables position-only implementation without dedicated velocity sensors. Closed-loop stability and finite-time convergence are proved via Lyapunov theory. Validation is entirely by numerical simulation on an experimentally identified second-order linear IPMC model. Within the 0.1–0.5 Hz biomimetic operating envelope, the proposed controller achieves an root mean square error (RMSE) of 1.07 μm at 0.5 Hz—approximately five times lower than the next best sliding mode controller (NTSMC, 5.18 μm)—while maintaining comparable chattering levels. The advantage is retained under $\pm 30\%$ parameter variations and external disturbances.

This is an open access article under the CC BY-SA license.

Corresponding Author:

Dhurgham R. M. Al-Tayar
Department of Electrical Engineering, Faculty of Engineering, University of Kufa
Najaf 54001, Iraq
Email: dhurghamr.hasan@uokufa.edu.iq

1. INTRODUCTION

Ionic polymer-metal composites (IPMCs) are smart electroactive-polymer actuators built from a thin Nafion or Flemion membrane with noble-metal electrodes, which bends when a low voltage (1–5 V) drives hydrated-cation migration toward the cathode [1], [2]. Their lightweight, flexible, biocompatible, silent operation makes them attractive for soft robotic manipulators and micro-grippers for precision assembly [3], [4], biomimetic underwater robots and fish-fin propulsion [5], [6], minimally invasive surgical end-effectors, and sensor-driven motion stages for biomedical-device manufacturing.

IPMCs are notoriously hard to control: their dynamics are simultaneously affected by nonlinearity, back-relaxation, hydration dependence, hysteresis, and resonance shift [7], on top of external disturbances (currents, turbulence, contact, temperature). A practical controller must therefore tolerate considerable parametric and exogenous uncertainty.

Various control strategies have been applied to IPMCs. Proportional–integral–derivative (PID) controllers [8] and impedance-based schemes [9] are simple to tune and perform adequately under mild condi-

tions. For stronger robustness, H_∞ synthesis [10], quantitative feedback theory [11], sliding mode control [12], [13], and robust PI synthesis [14] have been adopted; adaptive variants include iterative feedback tuning [15], inverse modelling [16], model-reference frameworks [17], and full-order recursive terminal sliding mode [18]. Recent IPMC-modelling advances include energy-based port-Hamiltonian formulations [19] and chemo-electromechanical models for engineered IPMCs [20]. Within the reviewed literature, few existing IPMC controllers simultaneously achieve fast convergence, smooth actuation, and robustness against both parametric uncertainty and external disturbances; this assessment is bounded by the works surveyed above and does not preclude unreported alternatives.

Sliding mode control (SMC) rejects matched disturbances by construction [21] but converges only asymptotically and chatters. Terminal SMC (TSMC) adds fractional-power terms for finite-time convergence [22], [23], with nonsingular variants avoiding the near-zero singularity [24]. Higher-order SMC (HOSM) relocates the discontinuity to a higher derivative of the sliding variable, keeping the control continuous [25], [26], [27]. Their combination—HOTSMC [28]—unites finite-time convergence with chattering suppression. The continuous third-order integral terminal SMC (3-ITSMC), demonstrated by Xu [29] on piezoelectric nanopositioning, drives s, $\dot{s}$, $\ddot{s}$ to zero simultaneously in finite time while the embedded integral term sharpens steady-state accuracy. Higher-order and terminal sliding mode schemes have since seen continued development for precision-actuator tracking, including fixed-time third-order super-twisting control [30] and fractional-order [31] and prescribed-performance [32] sliding mode designs for piezoelectric nanopositioning stages; these, however, target comparatively rigid piezoelectric stages rather than the strongly uncertain, back-relaxing IPMC plant considered here. No prior study has applied 3-ITSMC to IPMC soft actuators.

Table 1 positions the proposed controller against representative IPMC approaches from the survey above. The most direct comparison is the nonsingular terminal SMC (NTSMC) of Khawwaf *et al.* [7], [33], applied to the same identified second-order IPMC model used here. The 3-ITSMC differs from NTSMC in three concrete respects: i) Its discontinuity is integrated twice through the super-twisting structure and appears only on the third derivative of the sliding variable, so the control signal is continuous (NTSMC's sign-function discontinuity acts directly on the input); ii) The third-order design forces simultaneous finite-time convergence of s, $\dot{s}$, $\ddot{s}$, whereas a second-order terminal SMC enforces only s and $\dot{s}$; and iii) The integral term in the sliding surface adds persistent low-frequency disturbance compensation absent in NTSMC, reflected in the disturbance-rejection results of Section 3.

Table 1. Comparison of representative IPMC control approaches surveyed in this introduction. Each entry reflects the design and validation reported in the cited source.

Method [Ref.]	Finite-time convergence	Chattering reduction	Sliding order	Velocity sensor	Validation (cited)	Plant model assumed
PID [8]	No	—	—	Yes	Experimental	Identified
Conventional SMC [12]	No	Limited	1st	Yes	Simulation	Identified linear
NTSMC (Khawwaf *et al.*) [7], [33]	Yes	Moderate	1st	Yes	Experimental	2nd-order identified linear
Adaptive full-order recursive TSMC (Ekbatani *et al.*) [18]	Yes	Reduced	1st	Yes	Experimental	Identified linear
Proposed 3-ITSMC	Yes	Negligible (continuous control)	3rd	No (filtered derivative)	Simulation	2nd-order identified linear

This paper addresses the gap by developing a continuous 3-ITSMC for IPMC actuators and validating it through a multi-frequency numerical simulation study on the identified second-order linear IPMC model; experimental validation on a physical IPMC platform is identified as future work.

Accordingly, the objectives of this study are: i) To design a continuous third-order integral terminal sliding mode controller that delivers finite-time convergence and chattering-free actuation for the IPMC soft actuator; ii) To establish closed-loop stability and finite-time convergence via Lyapunov analysis, including the effect of position-only filtered-derivative estimation; and iii) To quantify tracking accuracy, chattering, and robustness against parametric uncertainty and external disturbances through a multi-frequency comparative simulation study against PID, conventional SMC, and NTSMC. The main contributions are:

a. The first application of 3-ITSMC to IPMC soft actuators, with quantitative evidence that the third-order integral terminal structure reduces tracking RMSE by approximately five times relative to NTSMC at 0.5 Hz under nominal conditions, with the advantage retained under $\pm 30\%$ parameter variations and external disturbances (see Section 3.).

b. An integrated position-only realization of the 3-ITSMC: velocity and acceleration are reconstructed by a filtered derivative scheme so that the controller requires only a single displacement sensor, and the closed-loop interaction between the estimator and the third-order super-twisting structure is treated within the stability analysis.
c. A multi-frequency comparative simulation study spanning 0.02–2.0 Hz against PID, conventional SMC, and NTSMC, in which the 3-ITSMC's advantage holds within the 0.1–0.5 Hz biomimetic operating envelope; behaviour outside this envelope is also characterised so that the operating limits are stated rather than implied.

The remainder of the paper presents the IPMC model and 3-ITSMC design in Section 2, the multi-frequency comparative simulation results in Section 3, and the conclusion in Section 4; full proofs are in Appendices A and B.

2. METHOD

2.1. IPMC model and input transformation

2.1.1. System description

Figure 1 shows the schematic of an IPMC actuator setup for underwater operation. The IPMC strip is vertically mounted in a water tank with one end fixed and the other free to deflect. When a voltage is applied across the electrodes, the IPMC bends due to the migration of hydrated cations within the polymer membrane. A laser position sensor is used to measure the tip displacement of the IPMC strip.

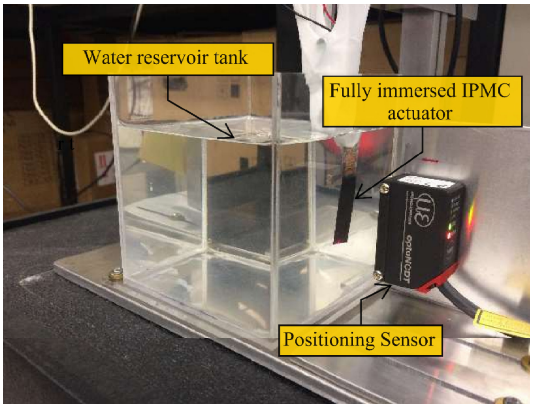

Figure 1. Schematic of the experimental setup for the underwater IPMC actuator system

2.1.2. Dynamic model

Due to the complex nonlinear behaviour of IPMC actuators, obtaining an accurate mathematical model is difficult, especially in underwater environments. In this work, a black-box modelling approach based on experimental identification is adopted [7], [33]. The input-output relationship of the IPMC actuator can be described by the following second-order differential equation:

$$m\ddot{y}(t) + b_0\dot{y}(t) + ky(t) = b_1\dot{u}(t) + b_2u(t) + \delta(t) + h(t) \tag{1}$$

where m, b_0, and k represent the equivalent mass, damping coefficient, and stiffness of the IPMC actuator respectively, $y(t)$ denotes the tip displacement output (in mm), $u(t)$ is the input voltage (in V), $\delta(t)$ represents external disturbances, and $h(t)$ accounts for system nonlinearities and unmodelled dynamics.

Following the general format of second-order systems, the model in (1) can be rewritten as:

$$\ddot{y} + a_1\dot{y} + a_2y = a_3\dot{u}(t) + a_4u(t) + d \tag{2}$$

where d represents the lumped uncertainties including nonlinear behaviour, modelling errors, parameter variations, and external disturbances. The system parameters are defined as $a_1 = b_0/m$, $a_2 = k/m$, $a_3 = b_1/m$, and $a_4 = b_2/m$.

Based on experimental identification conducted with the IPMC actuator fully immersed in water [33], the nominal system parameters are obtained as: $a_1 = 0.4357$ s^{-1}, $a_2 = 0.1219$ s^{-2}, $a_3 = 0.0031$ mm/(V·s), and $a_4 = 0.0146$ mm/(V·s^2).

Equations (1)–(2) are a *baseline* capturing the dominant dynamics about an operating point; hysteresis, creep, back-relaxation, nonlinearity, and parameter drift are absorbed into the lumped uncertainty d in (2). The controller is designed against the lumped bound (Assumption 1), and the $\pm 30\%$ parameter and step-disturbance tests in Section 3. cover this term.

2.1.3. Input transformation

It is noted from (2) that the model contains a derivative term $\dot{u}(t)$ of the control input, which must be handled carefully when dealing with discontinuous inputs such as step signals. For underwater IPMC applications that typically use continuous sinusoidal motions to mimic fish fin movement, a virtual control input is introduced as:

$$v(t) = a_3\dot{u}(t) + a_4u(t) \tag{3}$$

From (3), the actual control signal can be obtained through a low-pass filter by performing the Laplace transform:

$$u(s) = \frac{1}{a_3s + a_4}V(s) \tag{4}$$

Because a_3 and a_4 are both positive, the filter (4) is stable. Its single real pole at $s = -a_4/a_3 \approx -4.71$ rad/s (≈ 0.75 Hz cutoff) is low-pass with respect to $v(t)$: any residual switching content in $v(t)$ is attenuated before reaching the physical input $u(t)$, a structural advantage for chattering at the actuator level. The IPMC model (2) then simplifies to:

$$\ddot{y} + a_1\dot{y} + a_2y = v(t) + d \tag{5}$$

where $v(t)$ is the virtual control input that the 3-ITSMC will generate.

The following assumption is needed for the control design:

Assumption 1. The lumped disturbance d and its time derivative are bounded, i.e., $|d| \leq d_{\max}$ and $|\dot{d}| \leq \delta$, where $d_{\max}$ and δ are positive constants.

In practice, external disturbances on IPMC actuators—water currents, contact forces—are bounded in both magnitude and rate of change, so this assumption holds for typical operating conditions.

2.2. Design of 3-ITSMC controller

This section develops the 3-ITSMC for the IPMC actuator. Compared with conventional SMC, the design offers higher tracking precision, chattering-free actuation, and finite-time convergence.

2.2.1. Tracking error and filtered derivative estimation

Define the tracking error as:

$$e = y - y_r \tag{6}$$

Here y is the measured tip displacement and y_r the desired reference. We require y_r, $\dot{y}_r$, and $\ddot{y}_r$ to exist and be bounded—a condition met by the smooth sinusoidal trajectories common in IPMC applications.

Only position y is measured directly by the displacement sensor. Velocity and acceleration must therefore be reconstructed. A first-order low-pass filter provides smooth derivative estimates while suppressing measurement noise:

$$\dot{\hat{y}}_k = \alpha_f\dot{\hat{y}}_{k-1} + (1 - \alpha_f)\frac{y_k - y_{k-1}}{T} \tag{7}$$

Here $\alpha_f = \tau_d/(\tau_d + T)$ is the filter coefficient, τ_d the filter time constant, and T the sampling period.

Acceleration is then recovered by filtering the velocity estimate in the same way:

$$\ddot{\hat{y}}_k = \alpha_f \ddot{\hat{y}}_{k-1} + (1-\alpha_f)\frac{\dot{\hat{y}}_k - \dot{\hat{y}}_{k-1}}{T} \tag{8}$$

The recursions (7)–(8) are the discrete-time realisations of the continuous-time first-order low-pass dirty-differentiator transfer functions

$$H_v(s) = \frac{s}{\tau_d s + 1}, \qquad H_a(s) = \frac{s^2}{(\tau_d s + 1)^2}, \tag{9}$$

estimating $\dot{y}$, $\ddot{y}$ from $y(s)$ at $\mathcal{O}(1)$ per sample (embedded-friendly at the 1 kHz rate of Section 3.). Unlike raw backward differencing, which amplifies HF sensor noise by $\sim 1/T$, H_v and H_a roll off above $1/\tau_d$, keeping estimates bounded under realistic noise.

The low-pass structure of (9) also bounds the estimation errors used in the stability analysis of Section 2.3.:

Assumption 2. Let $e_v(t) := \dot{\hat{y}}(t) - \dot{y}(t)$ and $e_a(t) := \ddot{\hat{y}}(t) - \ddot{y}(t)$ be the filtered-derivative estimation errors produced by (7)–(8) (equivalently, (9)). For a band-limited reference y_r with bounded $\ddot{y}_r$ and measurement noise of bounded variance acting on y, there exist positive constants E_v, E_a, $\dot{E}_v$, $\dot{E}_a$ such that

$$|e_v(t)| \le E_v, \qquad |e_a(t)| \le E_a, \qquad |\dot{e}_v(t)| \le \dot{E}_v, \qquad |\dot{e}_a(t)| \le \dot{E}_a. \tag{10}$$

The deterministic contribution to these constants vanishes as $\tau_d \to 0$; the stochastic contribution scales with the sensor-noise standard deviation. Both contributions remain bounded for any finite $\tau_d > 0$.

2.2.2. Integral terminal sliding surface

The integral terminal sliding surface is defined as:

$$s = \lambda_1 e + \lambda_2 \int_0^t |e|^\alpha \mathrm{sign}(e)\, d\tau \tag{11}$$

where $\lambda_1 > 0$ and $\lambda_2 > 0$ are positive design gains, and the parameter α satisfies $1/2 < \alpha < 1$.

The time derivative of the sliding surface is:

$$\dot{s} = \lambda_1 \dot{e} + \lambda_2 |e|^\alpha \mathrm{sign}(e) \tag{12}$$

Theorem 1. *For the system plant given by* (5) *with the sliding surface* (11)*, once the sliding condition $\dot{s} = 0$ is enforced, the tracking error e converges to zero in finite time regardless of the initial state.*

Proof: See appendix A.

2.2.3. Control law design

The proposed virtual control law is designed as:

$$v(t) = u_{eq} + u_n \tag{13}$$

where u_{eq} is the equivalent controller and u_n is the nonlinear robust controller based on 3-ITSMC.

To derive the equivalent controller, taking the second derivative of the sliding surface (11) yields:

$$\ddot{s} = \lambda_1 \ddot{e} + \alpha\lambda_2 |e|^{\alpha-1}\dot{e} \tag{14}$$

When the sliding condition is satisfied (i.e., $\dot{s} = 0$), from (12) we have:

$$\dot{e} = -\frac{\lambda_2}{\lambda_1}|e|^\alpha \mathrm{sign}(e) \tag{15}$$

Substituting (15) into (14) gives:

$$\ddot{s} = \lambda_1 \ddot{e} - \frac{\alpha\lambda_2^2}{\lambda_1}|e|^{2\alpha-1}\mathrm{sign}(e) \tag{16}$$

The equivalent controller is designed as:

$$u_{eq} = \ddot{y}_r + a_1\dot{y} + a_2 y + \frac{\alpha\lambda_2^2}{\lambda_1^2}|e|^{2\alpha-1}\text{sign}(e) \tag{17}$$

The nonlinear robust controller is designed based on the third-order super-twisting algorithm:

$$u_n = -k_1|\Psi|^{1/2}\text{sign}(\Psi) + \phi \tag{18a}$$

$$\dot{\phi} = -k_2\text{sign}(\Psi) \tag{18b}$$

$$\Psi = \dot{s} + k_3|s|^{2/3}\text{sign}(s) \tag{18c}$$

where $k_1 > 0$, $k_2 > 0$, and $k_3 > 0$ are positive control gains. The exponent $2/3$ in (18c) is dictated by the homogeneity degree of the third-order sliding mode algorithm [34]: it ensures that Ψ has the correct scaling so that s, $\dot{s}$, and $\ddot{s}$ converge to zero simultaneously in finite time.

The complete 3-ITSMC control law is thus:

$$v = u_{eq} + u_n \tag{19}$$

The block diagram of the proposed 3-ITSMC control system is shown in Figure 2.

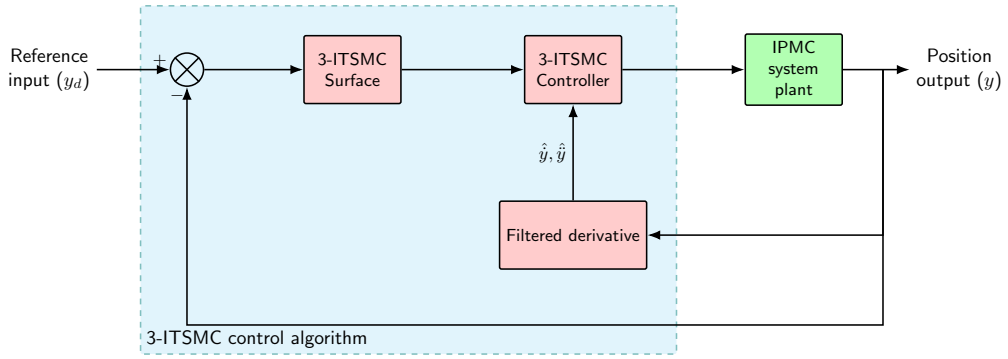

Figure 2. Block diagram of the proposed 3-ITSMC control strategy for IPMC actuator

The complete per-sample execution of the position-only 3-ITSMC, from the single displacement measurement to the physical voltage command, is summarised in Algorithm 1. Each step is $\mathcal{O}(1)$ in arithmetic and memory, so the loop is suitable for embedded microcontroller deployment.

Algorithm 1. Position-only 3-ITSMC update (one sample k)

Require: measurement y_k; reference $y_{r,k}, \dot{y}_{r,k}, \ddot{y}_{r,k}$; gains $\lambda_1, \lambda_2, \alpha, k_1, k_2, k_3$; filter coeff. α_f; states $\hat{\dot{y}}, \hat{\ddot{y}}, \phi, I_e, u$

$\hat{\dot{y}} \leftarrow \alpha_f\,\hat{\dot{y}} + (1-\alpha_f)(y_k - y_{k-1})/T$ ▷ filtered velocity, Eq. (7)

$\hat{\ddot{y}} \leftarrow \alpha_f\,\hat{\ddot{y}} + (1-\alpha_f)(\hat{\dot{y}} - \hat{\dot{y}}_{k-1})/T$ ▷ filtered acceleration, Eq. (8)

$e \leftarrow y_k - y_{r,k}$; $\dot{e} \leftarrow \hat{\dot{y}} - \dot{y}_{r,k}$ ▷ tracking error, Eq. (6)

$I_e \leftarrow I_e + |e|^{\alpha}\,\text{sign}(e)\,T$ ▷ integral term

$s \leftarrow \lambda_1 e + \lambda_2 I_e$; $\dot{s} \leftarrow \lambda_1\dot{e} + \lambda_2|e|^{\alpha}\text{sign}(e)$ ▷ surface, Eqs. (11)–(12)

$u_{eq} \leftarrow \ddot{y}_{r,k} + a_1\hat{\dot{y}} + a_2 y_k + (\alpha\lambda_2^2/\lambda_1^2)|e|^{2\alpha-1}\text{sign}(e)$ ▷ Eq. (17)

$\Psi \leftarrow \dot{s} + k_3|s|^{2/3}\text{sign}(s)$ ▷ Eq. (18c)

$\phi \leftarrow \phi - k_2\,\text{sign}(\Psi)\,T$; $u_n \leftarrow -k_1|\Psi|^{1/2}\text{sign}(\Psi) + \phi$ ▷ super-twisting, Eqs. (18a)–(18b)

$v \leftarrow u_{eq} + u_n$ ▷ virtual control, Eq. (19)

$u \leftarrow u + \big((v - a_4 u)/a_3\big)T$ ▷ recover physical voltage via LPF, Eq. (4)

return u

Remark 1. The proposed 3-ITSMC reduces to an ordinary third-order SMC (3-SMC) when the gain $\lambda_2 = 0$ is assigned. Hence, the 3-ITSMC has an additional integral action compared to the 3-SMC scheme, which contributes to improved tracking accuracy and disturbance rejection.

Remark 2. Convergence time depends on the initial condition and the gain ratio λ_2/λ_1. Raising this ratio speeds up convergence at the cost of possible overshoot, so the gains must be chosen with care.

Remark 3 (Gain selection procedure). The controller gains are selected according to the following procedure, in which each step ties to the equation that defines its feasibility region. No optimisation-based tuning is claimed; the procedure produces a stable initial choice that is then refined within those regions.

Step 1: *Sliding-surface gains* λ_1, λ_2, α. Choose $\alpha \in (0.5, 1)$ so the finite-time exponent $\eta = (\alpha + 1)/2$ lies in $(3/4, 1)$ as required by Theorem 1 (Appendix A). Choose $\lambda_1 > 0$ and $\lambda_2 > 0$ with the ratio λ_2/λ_1 trading convergence speed against overshoot per (15) and the settling-time bound (A.4).

Step 2: *Disturbance and estimation-error bounds.* Estimate the lumped-disturbance derivative bound δ (Assumption 1) and the estimation-error rate bound $\dot{E}_v$ (Assumption 2) for the operating condition; these bounds together drive the super-twisting condition in Step 3.

Step 3: *Super-twisting gains* k_1, k_2, k_3. Apply the sufficient conditions of [34]: k_2 must dominate the combined perturbation derivative bound,

$$k_2 \; > \; \delta + a_1 \, \dot{E}_v, \tag{20}$$

which is the modified form of the original $k_2 > \delta$ once the filtered-derivative estimation error is folded into the lumped disturbance (Section 2.3.); k_1 and k_3 are then selected large enough to ensure finite-time convergence of the cascaded super-twisting structure (B.4).

Step 4: *Filter time constant* τ_d. Choose τ_d from the noise level and the reference bandwidth so that the cutoff $1/\tau_d$ comfortably exceeds the reference bandwidth while attenuating sensor noise. The trade-off: smaller τ_d reduces phase lag (smaller E_v, E_a on the deterministic side) but admits more high-frequency noise.

Step 5: *Simulation refinement.* Verify the closed-loop response in simulation and adjust the gains within the feasible regions defined by Steps 1–4. The values used in this paper ($\lambda_1 = 10$, $\lambda_2 = 5$, $\alpha = 0.6$, $k_1 = 0.15$, $k_2 = 0.05$, $k_3 = 0.5$, with τ_d adapted to the test frequency in Section 2.4.) were obtained by this procedure and satisfy (20) for $\delta < 0.05$ of the IPMC model.

2.3. Stability analysis

The stability and finite-time convergence of the proposed 3-ITSMC are established by Lyapunov theory. Theorem 1 (stated in Section 2.2.) is proved in Appendix A; the proof of Theorem 2 below and the formal treatment of the filtered-derivative estimation error are given in Appendix B. The body of the paper retains the statements, the modified gain inequality (20), and a plain-language summary of each result.

Theorem 2. *For the system plant given by* (5) *with the sliding surface* (11) *and Assumption 1, if the control law is selected as* (19)*, then* $s = \dot{s} = \ddot{s} = 0$ *will be achieved in finite time. Consequently, the tracking error converges to zero in finite time.*

In plain terms: the cascaded super-twisting structure drives s, $\dot{s}$, $\ddot{s}$ to zero in finite time despite the bounded disturbance; Theorem 1 then delivers finite-time convergence of the tracking error. For the realistic filtered-derivative case (Assumption 2), the residual $a_1 e_v$ is absorbed into the lumped disturbance and the sufficient gain inequality tightens to $k_2 > \delta + a_1 \, \dot{E}_v$ (20), which holds with margin for the gains used here. Full derivations in Appendix B.

2.4. Simulation setup

In order to verify the effectiveness of the proposed 3-ITSMC, the simulation results are presented herein. For comparison purposes, four controllers are implemented: i) a PID controller, ii) a conventional SMC with discontinuous sign function (denoted SMC-sign), iii) a conventional SMC with boundary layer (denoted SMC-BL), and (iv) a nonsingular terminal SMC (NTSMC) based on the design in [7], which was applied to the same IPMC system.

The simulations are conducted in Python (NumPy for numerical computation, Matplotlib for plotting) with a fixed-step explicit forward-Euler integration of the plant (5) at a sampling time of $T = 0.001$ s (1 kHz); the controller, the filtered-derivative estimator (7)–(8), and the input low-pass filter (4) run at the same rate to reflect a realistic embedded implementation. The IPMC actuator model parameters are set to the identified values: $a_1 = 0.4357$ s^{-1}, $a_2 = 0.1219$ s^{-2}, $a_3 = 0.0031$ mm/(V·s), and $a_4 = 0.0146$ mm/(V·s^2).

To ensure realistic simulation conditions, measurement noise with a standard deviation of 1.0 μm is added to simulate the characteristics of typical displacement sensors used with IPMC actuators [7]. This noise level is consistent with the resolution of laser displacement sensors and capacitive probes in wet environments. In addition, the IPMC's back-relaxation effect is modelled with a time constant of 20 s and a gain of 5%, and an input delay of 4 samples (4 ms) is included to represent actuator response delays.

To assess the controllers across the operating range of biomimetic IPMC applications, the reference trajectory

$$y_r(t) = 0.05 \sin(2\pi f t) \text{ mm} \tag{21}$$

is tested at five frequencies: $f \in \{0.02, 0.1, 0.5, 1.0, 2.0\}$ Hz. The lowest frequency (0.02 Hz) represents slow positioning tasks, 0.1–0.5 Hz covers typical biomimetic fish-fin locomotion [6], and 1.0–2.0 Hz probes the upper bandwidth limit of IPMC actuators.

The filtered derivative time constant is adapted to the signal frequency as

$$\tau_d = \min\big(0.05,\ \max(0.002,\ 1/(20f))\big) \text{ s},$$

ensuring adequate noise rejection without excessive phase lag at higher frequencies. A smaller τ_d lowers the deterministic estimation-error bounds E_v, E_a (less phase lag) but admits more high-frequency sensor noise; the adapted rule keeps the cutoff $1/\tau_d$ comfortably above the reference bandwidth while preserving the stability margin required by the modified gain condition (20), so the closed loop remains well inside its finite-time-convergence region across the tested frequencies.

The control parameters for the proposed 3-ITSMC are selected as: $\lambda_1 = 10$, $\lambda_2 = 5$, $\alpha = 0.6$, $k_1 = 0.15$, $k_2 = 0.05$, and $k_3 = 0.5$. These gains are fixed across all frequencies to test the inherent robustness of the controller structure.

For the SMC-sign controller, a conventional sliding surface $s_c = c\,e + \dot{e}$ with $c = 7$ and a discontinuous sign-based reaching law is used with gains $k_1 = 0.08$ and $k_2 = 0.5$.

For the SMC-BL controller, the same sliding surface and gains are used, but the sign function is replaced by a saturation function with boundary layer width $\epsilon = 0.005$.

For the NTSMC controller, a nonsingular terminal sliding surface following the design in [33] is used: $s = e + \beta\,|\dot{e}|^{\gamma}\,\text{sign}(\dot{e})$ with $\beta = 1.5$ and $\gamma = 9/7$, with switching gain $\eta = 0.08$ and proportional gain $k_s = 0.5$.

The PID controller gains are tuned by minimising the integral of time-weighted absolute error (ITAE): $K_p = 25$, $K_i = 8$, and $K_d = 1.0$, with an anti-windup limit of 0.5.

The performance is evaluated using:

a. Root-mean-square error (RMSE): RMSE $= \sqrt{\frac{1}{N}\sum_{i=1}^{N}(y_r(i) - y(i))^2}$
b. Maximum absolute error: MaxError $= \max|y_r(i) - y(i)|$
c. Chattering metric: mean absolute control rate $|\overline{du/dt}|$ (V/s)

To obtain statistically meaningful comparisons, each test is repeated over $N = 30$ independent sensor-noise realizations (distinct pseudo-random seeds). All reported values of the three metrics above—RMSE, maximum absolute error, and the chattering metric—are the sample mean over these realizations, and every accompanying interval is a 95% confidence interval computed from the Student-t distribution ($\nu = 29$ degrees of freedom), not bootstrap resampling. Two uncertainty scenarios probe robustness. Parametric uncertainty is generated by scaling the identified damping and stiffness coefficients a_1 and a_2 by $\pm 30\%$ (i.e. factors 1.3 and 0.7); this range brackets the hydration-dependent parameter drift and partial-immersion effects reported for underwater IPMC actuators [7], [20], whose equivalent stiffness and damping vary substantially with water content and operating point. The external disturbance is a 10 μm (0.01 mm) displacement-equivalent step applied at the simulation midpoint—about 20% of the 50 μm motion amplitude—representing an abrupt contact force or current surge of the order encountered in the biomimetic operating environment. Both perturbations are bounded in magnitude and rate and therefore fall within the class covered by Assumption 1.

3. RESULTS AND DISCUSSION

3.1. Multi-frequency tracking performance

Table 2 reports nominal RMSE as mean ± 95% CI over $N = 30$ noise seeds (Student-t). At 0.02 Hz all means are below the 1 μm sensor-noise floor and are not practically meaningful despite tight CIs. Inside

the 0.1–0.5 Hz envelope the 3-ITSMC is decisive: at 0.5 Hz its $1.07 \pm 0.01\,\mu$m RMSE is $\approx 5\times$ lower than the next best (NTSMC, $5.18 \pm 0.01\,\mu$m) and $\approx 20\times$ lower than PID, separated by $>$100 CI half-widths — statistically and practically meaningful. Above 1 Hz the 3-ITSMC degrades below NTSMC and (at 2 Hz) below the conventional SMC variants; the controller-side mechanism is analysed in Section 3. Discussion, and the contribution is scoped to the 0.1–0.5 Hz envelope.

Table 2. Nominal RMSE (μm) vs. frequency, mean $\pm$ 95% confidence interval over $N = 30$ independent sensor-noise realizations.

Freq (Hz)	PID	SMC-sign	SMC-BL	NTSMC	3-ITSMC
0.02†	0.13±0.00	**0.12±0.00**	0.12±0.00	0.18±0.00	0.25±0.01
0.10	0.50±0.00	0.35±0.00	0.34±0.00	0.30±0.00	**0.24±0.01**
0.50	22.6±0.0	5.25±0.01	5.25±0.01	5.18±0.01	**1.07±0.01**
1.00	85.9±0.0	10.9±0.0	10.9±0.0	**7.89±0.05**	21.2±0.1
2.00	41.9±0.0	**16.5±0.0**	16.5±0.0	161±0	225±0

The chattering metric (Table 3) shows the 3-ITSMC is consistently smoothest or near-smoothest; at 1.0 Hz it generates $\sim$ 24 V/s vs. $\sim$ 171 V/s for SMC-sign (86% reduction). As shown in Figure 3, the box-plot of RMSE at 0.5 Hz over 30 independent noise realizations confirms that the proposed 3-ITSMC produces the lowest error distribution among the SMC-family controllers, while the corresponding numerical mean and confidence interval are reported in Table 2: the 3-ITSMC box at $\sim 1\,\mu$m sits well below the $\sim 5\,\mu$m boxes of NTSMC, SMC-sign and SMC-BL and far below PID ($\sim 22\,\mu$m), with negligible inter-seed dispersion.

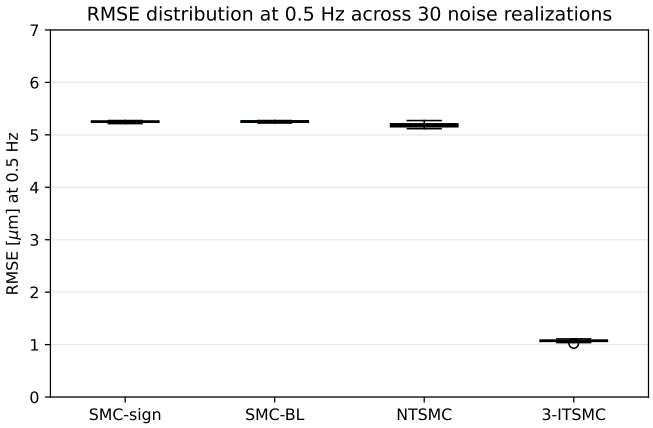

Figure 3. Box-plot of nominal RMSE at 0.5 Hz across $N = 30$ noise realizations for the four SMC-family controllers (PID omitted from the plot for scale clarity; its $\approx 22\,\mu$m RMSE is reported in Tables 2–4). Boxes are distinguished by hatch pattern rather than colour; median solid, mean dashed, box edges the 25%–75% quartiles, whiskers 1.5×IQR, outliers plotted separately

Figure 4 summarises the full 0.02–2.0 Hz sweep as grouped bar charts: Figure 4(a) shows nominal RMSE and Figure 4(b) shows the chattering metric, for all five controllers. The advantage of the 3-ITSMC within the 0.1–0.5 Hz envelope and its degradation above 1 Hz are both visible at a glance, consistent with Tables 2 and 3.

3.2. Detailed analysis at 0.5 Hz

Because 0.5 Hz falls in the typical range of biomimetic fish-fin locomotion [5], [6], this subsection examines the controller behaviour in detail at this frequency.

Figure 5 shows tracking under nominal conditions for one representative seed (per-seed dispersion of the headline RMSE is in Figure 3) and should be read together with the statistical RMSE results in Table 2. PID fails the reference; SMC-sign, SMC-BL and NTSMC track with visible offset. The maximum absolute steady-state error confirms this over the full seed set: $1.88 \pm 0.06\,\mu$m for the 3-ITSMC against $7.74 \pm 0.05\,\mu$m (NTSMC), $7.51 \pm 0.03\,\mu$m (SMC-sign), $7.51 \pm 0.02\,\mu$m (SMC-BL) and $32.7 \pm 0.0\,\mu$m (PID), so the worst-case

excursion follows the same ordering as the RMSE rather than being driven by isolated peaks. Control-signal magnitudes are consistent with Table 3, and the small, actuator-safe control signals of the 3-ITSMC are directly relevant to precision positioning and soft-gripper tasks, where high-frequency switching would damage the polymer membrane.

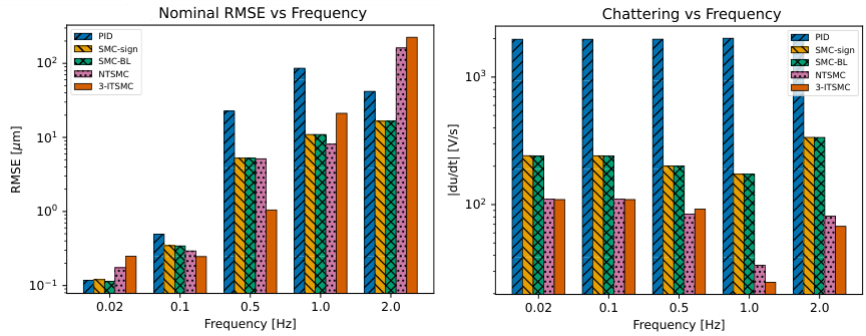

(a) (b)

Figure 4. Multi-frequency summary over the 0.02–2.0 Hz sweep (a) nominal RMSE (logarithmic scale) and (b) chattering metric $|\overline{du/dt}|$ versus frequency for all five controllers (grouped bars, means over $N = 30$ noise realizations). Controllers are distinguished by bar texture rather than colour; numerical values with 95% CIs are in Tables 2 and 3

Table 3. Chattering metric $|\overline{du/dt}|$ (V/s) vs. frequency, mean $\pm$ 95% confidence interval over $N = 30$ independent sensor-noise realizations

Freq (Hz)	PID	SMC-sign	SMC-BL	NTSMC	3-ITSMC
0.02	1978±2.0	242±0.2	241±0.2	110±0.1	**110±0.1**
0.10	1978±2.0	242±0.2	241±0.2	110±0.1	**110±0.1**
0.50	1977±6.9	200±0.6	200±0.6	**85±0.3**	92±0.3
1.00	1977±7.4	171±0.6	170±0.6	32±0.2	**24±0.1**
2.00	1990±9.4	334±1.3	334±1.3	81±0.3	**68±0.1**

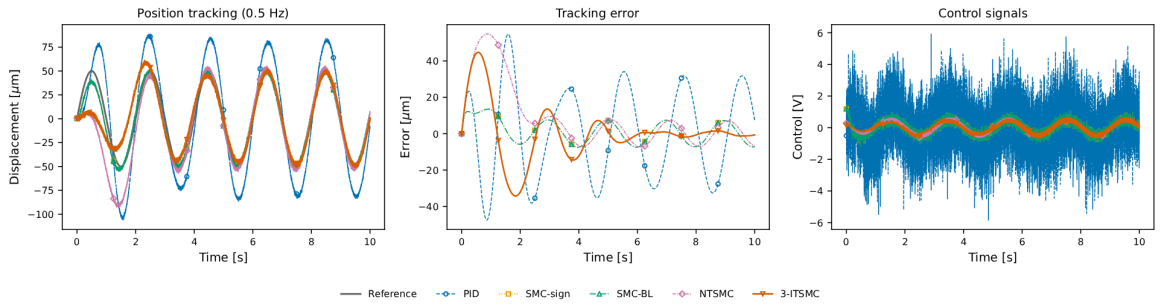

Figure 5. Representative single-seed simulation at 0.5 Hz position tracking, tracking error, and control signals. This figure shows one representative run; the statistical RMSE (mean $\pm$ 95% CI over $N = 30$ seeds) is reported in Table 2 and Figure 3

Figure 6 compares the zoomed steady-state control signals at 0.5 Hz and supports the chattering analysis reported in Table 3, showing that the proposed 3-ITSMC generates a smoother control input than the discontinuous SMC-based controllers. The difference in control signal quality is evident: the SMC-sign and PID produce high-frequency oscillations that would cause electrode delamination and polymer degradation in physical IPMC actuators, while the 3-ITSMC generates smooth, actuator-safe control signals—a decisive advantage for the durability of soft robotic actuators driven continuously in service.

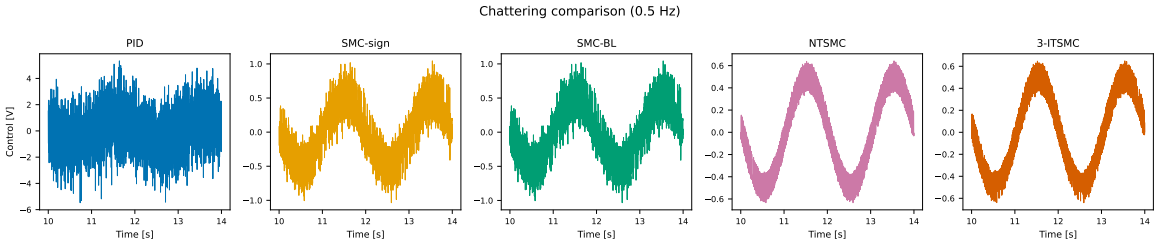

Figure 6. Representative zoomed steady-state control signals at 0.5 Hz for all five controllers; the corresponding mean chattering metric $\overline{|du/dt|}$ over $N = 30$ seeds is reported in Table 3. Signal smoothness is the actuator-safety criterion for continuously driven soft grippers and precision positioning stages

3.3. Robustness against uncertainties

To verify the robustness of the proposed controller, the tracking performance at 0.5 Hz is tested under $\pm 30\%$ model parameter variations, representing conditions where the IPMC is partially immersed or where environmental conditions have changed.

Figures 7(a) and 7(b) show representative tracking errors under $+30\%$ and -30% parameter variations at 0.5 Hz, respectively, and should be discussed together with the mean RMSE and 95% confidence intervals reported in Table 4. Under $+30\%$ parameter variation, the 3-ITSMC achieves an RMSE of 0.90 ± 0.01 μm, while the NTSMC and SMC-sign degrade to 5.08 ± 0.01 μm and 5.14 ± 0.01 μm, respectively. Under -30% variation, the 3-ITSMC reaches 1.89 ± 0.04 μm versus 5.54 ± 0.02 μm (NTSMC) and 5.41 ± 0.01 μm (SMC-sign). Table 4 shows that this robustness advantage holds across all frequencies inside the 0.1–0.5 Hz envelope—an essential property for IPMC actuators whose stiffness drifts with hydration during sustained operation.

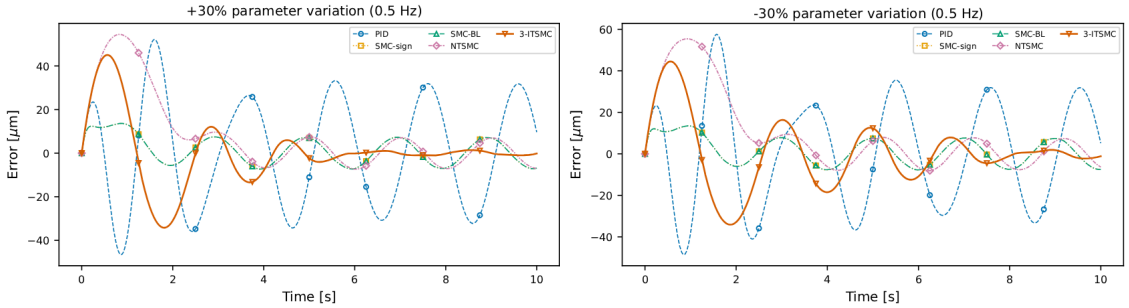

(a) (b)

Figure 7. Representative tracking error at 0.5 Hz under (a) $+30\%$ and (b) -30% parameter variations. This figure shows one representative run; the mean RMSE with 95% CI over $N = 30$ seeds is reported in Table 4. The two panels quantify tolerance to the hydration-driven stiffness drift of IPMC actuators in sustained underwater operation

Table 4. RMSE (μm) vs. frequency under the two perturbation scenarios, mean $\pm$ 95% CI ($N = 30$): (a) $+30\%$ parameter uncertainty; (b) a 10 μm step disturbance applied at the simulation midpoint

	(a) $+30\%$ parameter uncertainty					(b) 10 μm step disturbance				
Freq (Hz)	PID	SMC-sign	SMC-BL	NTSMC	3-ITSMC	PID	SMC-sign	SMC-BL	NTSMC	3-ITSMC
0.02	**0.13±0.00**	0.15±0.00	0.14±0.00	0.22±0.00	0.23±0.01	0.14±0.00	0.39±0.00	0.38±0.00	0.76±0.01	**0.24±0.01**
0.10	0.55±0.00	0.41±0.00	0.41±0.00	0.46±0.01	**0.22±0.01**	0.51±0.00	0.50±0.00	0.50±0.00	0.82±0.01	**0.24±0.01**
0.50	22.6±0.0	5.14±0.01	5.14±0.00	5.08±0.01	**0.90±0.01**	22.6±0.0	5.28±0.01	5.29±0.01	5.36±0.01	**1.07±0.01**
1.00	84.2±0.0	10.6±0.0	10.6±0.0	**7.49±0.05**	12.7±0.0	85.9±0.0	10.9±0.0	10.9±0.0	**9.44±0.06**	21.6±0.1
2.00	41.8±0.0	**16.3±0.0**	16.3±0.0	146±0	177±0	41.9±0.0	**16.2±0.0**	16.2±0.0	160±0	230±0

3.4. Disturbance rejection

A step disturbance of 0.01 mm (10 μm) is applied at the simulation midpoint to test disturbance rejection. Table 4 shows the disturbance RMSE across frequencies.

At 0.5 Hz, the 3-ITSMC maintains an RMSE of 1.07 ± 0.01 μm under disturbance—essentially unchanged from the nominal case (1.07 ± 0.01 μm)—while the other SMC controllers degrade to 5.28–5.36 μm. At 0.1 Hz, the advantage is even more pronounced: the 3-ITSMC achieves 0.24 ± 0.01 μm versus 0.50 ± 0.00 μm (SMC-sign) and 0.82 ± 0.01 μm (NTSMC). The integral term in the sliding surface (11) provides persistent low-frequency compensation that effectively rejects step-type disturbances without increasing chattering.

3.5. Discussion

The multi-frequency results reveal four findings.

First, within the 0.1–0.5 Hz envelope the 3-ITSMC reaches $\approx 5\times$ lower RMSE than the next best controller at 0.5 Hz (Table 2); the integral terminal surface drives this advantage, which is most effective when the period is long enough for the integral to build up. Robustness at 0.5 Hz inside the envelope is preserved: $\approx 5\times$ at $+30\%$ uncertainty and under step disturbance, $\approx 3\times$ at -30% (Table 4).

Second, chattering reduction is 54–86% relative to SMC-sign across all frequencies; at 1.0 Hz the 3-ITSMC has the lowest chattering of all controllers (24 vs. 171 V/s), a practical advantage for IPMC longevity given the heating, delamination, and polymer degradation caused by HF switching.

Third, the tracking advantage does not extend above $\sim$ 1 Hz. Three controller-side causes: (a) the fixed gain set is tuned for 0.1–0.5 Hz and not rescheduled; (b) the integral action (11) adds phase lag that becomes detrimental once the period approaches the settling time; (c) the terminal exponent $2\alpha - 1$ in (17) is ill-conditioned at higher frequencies. Plant bandwidth contributes but is not the sole cause. Tables 2–4 show NTSMC outperforms the 3-ITSMC at 1 Hz and the 3-ITSMC degrades below the conventional SMC variants at 2 Hz. The contribution is scoped to the 0.1–0.5 Hz envelope; 1–2 Hz operation would need frequency-scheduled gains, identified as future work.

Fourth, learning-based methods—RL for soft actuators [35], Koopman MPC [36], and NN-MPC [37]—can absorb unmodelled dynamics from data, at the cost of training/identification effort, runtime overhead, and lost closed-form stability guarantees. For embedded low-power IPMC control, the proposed 3-ITSMC's analytic robustness at $\mathcal{O}(1)$ per-step cost is a deliberate trade-off; the two approach families are complementary.

4. CONCLUSION

A multi-frequency numerical simulation study (0.02–2.0 Hz, $N = 30$ noise seeds) compares the proposed 3-ITSMC with PID, conventional SMC, and NTSMC under nominal, $\pm 30\%$ parametric, and step-disturbance conditions. Within the 0.1–0.5 Hz biomimetic operating envelope, the key findings are:

a. The 3-ITSMC achieves the lowest tracking error of the compared controllers; at 0.5 Hz it reaches an RMSE of 1.07 ± 0.01 μm over $N = 30$ noise realizations—approximately five times lower than the next best SMC controller, NTSMC (Table 2).
b. The chattering reduction is consistent across all frequencies (54–86% versus SMC-sign), with the 3-ITSMC producing actuator-safe control signals that protect the IPMC against premature degradation.
c. Under $\pm 30\%$ parameter variations and step disturbances the 3-ITSMC retains an approximately five-fold tracking advantage at 0.5 Hz (Table 4), confirming robustness.
d. Above 1 Hz, the 3-ITSMC tracking degrades because the fixed gain set is tuned for the envelope and the integral action introduces phase lag (full analysis in Section 3.); chattering nevertheless remains the lowest of all controllers. Frequency-scheduled gains are identified as future work.

The controller is computationally lightweight: each step is $\mathcal{O}(1)$ arithmetic (one super-twisting update + two first-order filters) with constant memory, suitable for embedded microcontroller deployment in soft grippers, compliant end-effectors, and precision positioning stages. Two deployment caveats: performance is sensitive to sampling rate (filter cutoff $1/\tau_d$ must exceed closed-loop bandwidth) and to actuation latency (modelled as 4-sample delay).

Limitations: i) validation is simulation-based on a linear baseline model with hysteresis, creep, and ionic diffusion absorbed into the lumped disturbance; ii) the formal stability extension (Appendix B) covering

filtered-derivative estimation error under condition (20) is analytic only, not yet experimentally corroborated; iii) controller gains are fixed across frequencies.

Open problems and future work: i) experimental validation on a physical IPMC platform, including embedded deployment on microcontroller hardware; ii) frequency-scheduled / adaptive gains for 1–2 Hz operation; iii) extension to multi-DOF and multi-segment IPMC systems for precision micro-positioning, soft robotic manipulation, and automated assembly, where the segment-coupling dynamics are not captured by the lumped-uncertainty term; and iv) robustness to underwater disturbances outside the bounded class of Assumption 1 (impulsive contact, current surges).

ACKNOWLEDGMENTS

The authors would like to thank the University of Kufa and Al-Mustaqbal University for supporting this research.

FUNDING INFORMATION

Authors state no funding involved.

AUTHOR CONTRIBUTIONS STATEMENT

This journal uses the Contributor Roles Taxonomy (CRediT) to recognize individual author contributions, reduce authorship disputes, and facilitate collaboration.

Name of Author	C	M	So	Va	Fo	I	R	D	O	E	Vi	Su	P	Fu
Dhurgham R.M. AL-Tayar	✓			✓	✓	✓		✓	✓	✓	✓		✓	
Ali Al-Ghanimi	✓	✓	✓	✓	✓	✓			✓	✓		✓		
Ibrahim H. Al-Kharsan		✓		✓		✓	✓			✓	✓			

C : **C**onceptualization
M : **M**ethodology
So : **So**ftware
Va : **Va**lidation
Fo : **Fo**rmal Analysis
I : **I**nvestigation
R : **R**esources
D : **D**ata Curation
O : Writing - **O**riginal Draft
E : Writing - Review & **E**diting
Vi : **Vi**sualization
Su : **Su**pervision
P : **P**roject Administration
Fu : **Fu**nding Acquisition

CONFLICT OF INTEREST STATEMENT

Authors state no conflict of interest.

DATA AVAILABILITY

The simulation data and Python code are available from the corresponding author upon reasonable request.

REFERENCES

[1] J. Lai *et al.*, "Current research status of ionic polymer-metal composites in applications of low-voltage actuators," *Materials Advances*, vol. 5, no. 11, pp. 4601–4617, 2024, doi: 10.1039/D4MA00040D.

[2] S. Nemat-Nasser and J. Y. Li, "Electromechanical response of ionic polymer-metal composites," *Journal of Applied Physics*, vol. 87, no. 7, pp. 3321–3331, Apr. 2000, doi: 10.1063/1.372343.

[3] K. Aw and A. McDaid, "Bio-applications of ionic polymer metal composite transducers," *Smart Materials and Structures*, vol. 23, no. 7, p. 074005, Jul. 2014, doi: 10.1088/0964-1726/23/7/074005.

[4] J. Santos, B. Lopes, and P. C. Branco, "Ionic polymer-metal composite material as a diaphragm for micropump devices," *Sensors and Actuators A: Physical*, vol. 161, no. 1–2, pp. 225–233, Jun. 2010, doi: 10.1016/j.sna.2010.04.032.

[5] D. Q. Truong, K. K. Ahn, D. N. C. Nam, and J. I. Yoon, "Identification of a nonlinear black-box model for a self-sensing polymer metal composite actuator," *Smart Materials and Structures*, vol. 19, no. 8, p. 085015, Aug. 2010, doi: 10.1088/0964-1726/19/8/085015.

[6] M. Aureli, V. Kopman, and M. Porfiri, "Free-locomotion of underwater vehicles actuated by ionic polymer metal composites," *IEEE/ASME Transactions on Mechatronics*, vol. 15, no. 4, pp. 603–614, Aug. 2010, doi: 10.1109/TMECH.2009.2030887.

[7] J. Khawwaf, J. Zheng, R. Lu, A. Al-Ghanimi, B. I. Kazem, and Z. Man, "Robust tracking control of an IPMC actuator using nonsingular terminal sliding mode," *Smart Materials and Structures*, vol. 26, no. 9, art. no. 095042, Aug. 2017, doi: 10.1088/1361-665X/aa7d69.

[8] B.-K. Fang, M.-S. Ju, and C.-C. K. Lin, "A new approach to develop ionic polymer-metal composites (IPMC) actuator: Fabrication and control for active catheter systems," *Sensors and Actuators A: Physical*, vol. 137, no. 2, pp. 321–329, Jul. 2007, doi: 10.1016/j.sna.2007.03.024.

[9] R. C. Richardson, M. C. Levesley, M. D. Brown, J. A. Hawkes, K. Watterson, and P. G. Walker, "Control of ionic polymer metal composites," *IEEE/ASME Transactions on Mechatronics*, vol. 8, no. 2, pp. 245–253, Jun. 2003, doi: 10.1109/TMECH.2003.812835.

[10] S. Kang, J. Shin, S. J. Kim, H. J. Kim, and Y. H. Kim, "Robust control of ionic polymer-metal composites," *Smart Materials and Structures*, vol. 16, no. 6, pp. 2457–2463, Dec. 2007, doi: 10.1088/0964-1726/16/6/049.

[11] H. Moeinkhah, A. Akbarzadeh, and J. Rezaeepazhand, "Design of a robust quantitative feedback theory position controller for an ionic polymer metal composite actuator using an analytical dynamic model," *Journal of Intelligent Material Systems and Structures*, vol. 25, no. 15, pp. 1965–1977, Oct. 2014, doi: 10.1177/1045389X13512906.

[12] D. Wang, Q. Zhang, and A. Wang, "Robust nonlinear control design for ionic polymer metal composite based on sliding mode approach," in *Proceedings of the UKACC International Conference on Control*, Loughborough, U.K., Jul. 2014, pp. 519–524, doi: 10.1109/CONTROL.2014.6915194.

[13] J. Khawwaf, J. Zheng, R. Chai, R. Lu, and Z. Man, "Adaptive microtracking control for an underwater IPMC actuator using new hyperplane-based sliding mode," *IEEE/ASME Transactions on Mechatronics*, vol. 24, no. 5, pp. 2108–2117, Oct. 2019, doi: 10.1109/TMECH.2019.2937328.

[14] R. M. Kagami, R. C. Freire, and G. Reynoso-Meza, "Multiobjective robust PI synthesis in plants with uncertain poles," *IFAC-PapersOnLine*, vol. 58, no. 7, pp. 174–179, 2024, doi: 10.1016/j.ifacol.2024.08.030.

[15] D. Liu, A. McDaid, K. Aw, and S. Xie, "Position control of an ionic polymer metal composite actuated rotary joint using iterative feedback tuning," *Mechatronics*, vol. 21, no. 1, pp. 315–328, Feb. 2011, doi: 10.1016/j.mechatronics.2010.12.001.

[16] L. Hao and Z. Li, "Modeling and adaptive inverse control of hysteresis and creep in ionic polymer-metal composite actuators," *Smart Materials and Structures*, vol. 19, no. 2, p. 025014, Feb. 2010, doi: 10.1088/0964-1726/19/2/025014.

[17] X. Chen and C.-Y. Su, "Adaptive control for ionic polymer-metal composite actuators," *IEEE Transactions on Systems, Man, and Cybernetics: Systems*, vol. 46, no. 10, pp. 1468–1477, Oct. 2016, doi: 10.1109/TSMC.2016.2523921.

[18] R. Z. Ekbatani, K. Shao, J. Khawwaf, H. Wang, J. Zheng, X. Chen, and M. Nikzad, "Control of an IPMC soft actuator using adaptive full-order recursive terminal sliding mode," *Actuators*, vol. 10, no. 2, p. 33, Feb. 2021, doi: 10.3390/act10020033.

[19] N. Liu, Y. Wu, and Y. Le Gorrec, "Energy-based modeling of ionic polymer–metal composite actuators dedicated to the control of flexible structures," *IEEE/ASME Transactions on Mechatronics*, vol. 26, no. 6, pp. 3139–3150, Dec. 2021, doi: 10.1109/TMECH.2021.3053609.

[20] O. Fakharian, W. S. Nagel, K. K. Leang, and M. Aureli, "Engineered ionic polymer metal composites (eIPMCs) under dynamic compression loading conditions: Theory and experiments," *Smart Materials and Structures*, vol. 34, no. 2, p. 025048, Feb. 2025, doi: 10.1088/1361-665X/adaab6.

[21] V. I. Utkin, *Sliding modes in control and optimization*. Berlin, Germany: Springer-Verlag, 1992.

[22] Y. Wu, X. Yu, and Z. Man, "Terminal sliding mode control design for uncertain dynamic systems," *Systems & Control Letters*, vol. 34, no. 5, pp. 281–287, Jul. 1998, doi: 10.1016/S0167-6911(98)00036-X.

[23] X. Yu and Z. Man, "Fast terminal sliding-mode control design for nonlinear dynamical systems," *IEEE Transactions on Circuits and Systems I: Fundamental Theory and Applications*, vol. 49, no. 2, pp. 261–264, Feb. 2002, doi: 10.1109/81.983876.

[24] Y. Feng, X. Yu, and Z. Man, "Non-singular terminal sliding mode control of rigid manipulators," *Automatica*, vol. 38, no. 12, pp. 2159–2167, Dec. 2002, doi: 10.1016/S0005-1098(02)00147-4.

[25] A. Levant, "Higher-order sliding modes, differentiation and output-feedback control," *International Journal of Control*, vol. 76, no. 9–10, pp. 924–941, 2003, doi: 10.1080/0020717031000099029.

[26] A. Levant, "Principles of 2-sliding mode design," *Automatica*, vol. 43, no. 4, pp. 576–586, Apr. 2007, doi: 10.1016/j.automatica.2006.10.008.

[27] E. Cruz-Zavala and J. A. Moreno, "High-order sliding-mode control design homogeneous in the bi-limit," *International Journal of Robust and Nonlinear Control*, vol. 31, no. 9, pp. 3380–3416, Jun. 2021, doi: 10.1002/rnc.5242.

[28] Q. Xu, "Digital integral terminal sliding mode predictive control of piezoelectric-driven motion system," *IEEE Transactions on Industrial Electronics*, vol. 63, no. 6, pp. 3976–3984, Jun. 2016, doi: 10.1109/TIE.2015.2504343.

[29] Q. Xu, "Continuous integral terminal third-order sliding mode motion control for piezoelectric nanopositioning system," *IEEE/ASME Transactions on Mechatronics*, vol. 22, no. 4, pp. 1828–1838, Aug. 2017, doi: 10.1109/TMECH.2017.2701417.

[30] G. Wang, B. Wang, and C. Zhang, "Fixed-time third-order super-twisting-like sliding mode motion control for piezoelectric nanopositioning stage," *Mathematics*, vol. 9, no. 15, art. no. 1770, Jul. 2021, doi: 10.3390/math9151770.

[31] R. Xu, Z. Wang, M. Zhou, and D. Tian, "A robust fractional-order sliding mode control technique for piezoelectric nanopositioning stages in trajectory-tracking applications," *Sensors and Actuators A: Physical*, vol. 363, art. no. 114711, Nov. 2023, doi: 10.1016/j.sna.2023.114711.

[32] S. Wen, S. Zhang, and J. Yu, "Prescribed-performance-based sliding mode control for piezoelectric actuator systems," *Actuators*, vol. 14, no. 11, art. no. 516, Nov. 2025, doi: 10.3390/act14110516.

[33] J. Khawwaf, J. Zheng, R. Lu, A. Al-Ghanimi, B. I. Kazem, and Z. Man, "Robust terminal sliding mode control of IPMC actuators," in *Proceedings of the IEEE 56th Annual Conference on Decision and Control (CDC)*, Melbourne, VIC, Australia, Dec. 2017, pp. 3295–3300, doi: 10.1109/CDC.2017.8264143.

[34] S. Kamal, A. Chalanga, J. A. Moreno, L. Fridman, and B. Bandyopadhyay, "Higher order super-twisting algorithm," in *Proceedings of the 13th IEEE Workshop on Variable Structure Systems (VSS)*, Nantes, France, Jun./Jul. 2014, pp. 1–5, doi: 10.1109/VSS.2014.6881129.

[35] T. G. Thuruthel, E. Falotico, F. Renda, and C. Laschi, "Model-based reinforcement learning for closed-loop dynamic control of soft robotic manipulators," *IEEE Transactions on Robotics*, vol. 35, no. 1, pp. 124–134, Feb. 2019, doi: 10.1109/TRO.2018.2878318.

[36] D. Bruder, X. Fu, R. B. Gillespie, C. D. Remy, and R. Vasudevan, "Data-driven control of soft robots using Koopman operator

theory," *IEEE Transactions on Robotics*, vol. 37, no. 3, pp. 948–961, Jun. 2021, doi: 10.1109/TRO.2020.3038693.
[37] M. T. Gillespie, C. M. Best, E. C. Townsend, D. Wingate, and M. D. Killpack, "Learning nonlinear dynamic models of soft robots for model predictive control with neural networks," in *Proceedings of the IEEE International Conference on Soft Robotics (RoboSoft)*, Livorno, Italy, Apr. 2018, pp. 39–45, doi: 10.1109/ROBOSOFT.2018.8404894.
[38] S. P. Bhat and D. S. Bernstein, "Finite-time stability of continuous autonomous systems," *SIAM Journal on Control and Optimization*, vol. 38, no. 3, pp. 751–766, 2000, doi: 10.1137/S0363012997321358.
[39] S. Kamal, J. A. Moreno, A. Chalanga, B. Bandyopadhyay, and L. M. Fridman, "Continuous terminal sliding-mode controller," *Automatica*, vol. 69, pp. 308–314, Jul. 2016, doi: 10.1016/j.automatica.2016.02.001.

APPENDIX A. PROOF OF THEOREM 1

Consider the Lyapunov function candidate

$$V = \tfrac{1}{2}e^2, \tag{A.1}$$

whose time derivative is $\dot{V} = e\,\dot{e}$. Assuming $\dot{s} = 0$, (12) gives

$$\dot{e} = -\tfrac{\lambda_2}{\lambda_1}\,|e|^{\alpha}\,\mathrm{sign}(e), \tag{A.2}$$

so that

$$\dot{V} = -\tfrac{\lambda_2}{\lambda_1}\,|e|^{\alpha+1} \;\le\; -2^{(\alpha+1)/2}\tfrac{\lambda_2}{\lambda_1}\,V^{(\alpha+1)/2}. \tag{A.3}$$

Hence $\dot{V} + \rho V^{\eta} \le 0$ with $\rho = 2^{(\alpha+1)/2}\lambda_2/\lambda_1$ and $\eta = (\alpha+1)/2$. Since $1/2 < \alpha < 1$, $\eta \in (3/4,\,1)$, and finite-time stability [38] yields the settling-time bound

$$T_s \le \frac{V^{1-\eta}(e_0)}{\rho\,(1-\eta)}. \tag{A.4}$$

This completes the proof. □

APPENDIX B. PROOF OF THEOREM 2 AND TREATMENT OF DERIVATIVE-ESTIMATION ERROR

From the error dynamics,

$$\ddot{e} = -a_1\dot{y} - a_2 y + v + d - \ddot{y}_r. \tag{B.1}$$

Substituting (19) with (17) gives

$$\ddot{e} = -u_n + d. \tag{B.2}$$

Substituting (B.2) into (16) and using the robust control law (18) produces, after algebra,

$$\ddot{s} = -\lambda_1 k_1\,|\Psi|^{1/2}\,\mathrm{sign}(\Psi) + p, \tag{B.3a}$$

$$\dot{p} = -k_2\lambda_1\,\mathrm{sign}(\Psi) + \lambda_1\dot{d}, \tag{B.3b}$$

where $p = \lambda_1(\phi + d)$. Setting $\sigma_1 = s$, $\sigma_2 = \dot{s}$, these become

$$\begin{aligned} \dot{\sigma}_1 &= \sigma_2, & \dot{\sigma}_2 &= -\lambda_1 k_1\,|\Psi|^{1/2}\,\mathrm{sign}(\Psi) + p, \\ \dot{p} &= -k_2\lambda_1\,\mathrm{sign}(\Psi) + \lambda_1\dot{d}, & \Psi &= \sigma_2 + k_3\,|\sigma_1|^{2/3}\,\mathrm{sign}(\sigma_1), \end{aligned} \tag{B.4a}$$

which has the cascaded super-twisting structure of [25], [34]. With $|\lambda_1\dot{d}| \le \delta\lambda_1$ (Assumption 1), the result of [34], [39] provides finite-time convergence of σ_1, σ_2 and p to zero under $k_2 > \delta$ and sufficiently large k_1, k_3. The gains $\lambda_1 = 10$, $k_1 = 0.15$, $k_2 = 0.05$, $k_3 = 0.5$ used in this paper satisfy $k_2\lambda_1 = 0.5 > \delta\lambda_1$ for the estimated bound $\delta < 0.05$. Differentiating (B.3a) shows $\ddot{s}$ also converges in finite time, with s, $\dot{s}$, $\ddot{s}$ continuous and $\dddot{s}$ discontinuous through $-k_2\lambda_1\,\mathrm{sign}(\Psi)$. By Theorem 1, e and $\dot{e}$ then reach zero in finite time.

For the realised controller, the filtered estimates of (7)–(8) replace $\dot{y}$, $\ddot{y}$ in u_{eq} (17); Assumption 2 provides $|e_v|, |e_a|, |\dot{e}_v|, |\dot{e}_a|$ bounded by E_v, E_a, $\dot{E}_v$, $\dot{E}_a$. The substitution $\hat{y} = \dot{y} + e_v$ in (17) adds a residual $a_1 e_v$ that does not cancel in (B.1), so (B.2) becomes

$$\ddot{e} = -u_n + d + a_1 e_v \;=:\; -u_n + \tilde{d}, \tag{B.5}$$

with $|\dot{\tilde{d}}(t)| \le \delta + a_1\,\dot{E}_v =: \tilde{\delta}$. The cascaded super-twisting analysis above carries through with $\tilde{\delta}$ replacing δ, tightening the sufficient condition to

$$k_2 > \delta + a_1\,\dot{E}_v, \tag{B.6}$$

matching (20) in the gain-selection procedure. Provided (B.6) holds and τ_d is small enough that $1/\tau_d$ comfortably exceeds the closed-loop bandwidth, the conclusion of Theorem 2 is preserved: the inherent bounded-perturbation robustness of the super-twisting algorithm [39] absorbs the filtered-derivative estimation error. The numerical values used in this paper satisfy (B.6) with margin, consistent with the chattering-free behaviour observed in section 3.

BIOGRAPHIES OF AUTHORS

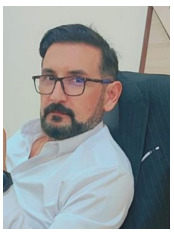

Dhurgham R. M. Al-Tayar received his Ph.D. degree from the College of Engineering, Department of Control and Systems Engineering, University of Baghdad, in 2023. He obtained his M.Sc. degree from the same university and department in 2015, Iraq. He is currently a lecturer in the Department of Electrical Engineering, College of Engineering, University of Kufa. His research interests include control systems and computer engineering. He has published numerous research papers in both local and international journals in the field of control and computer engineering. He can be contacted via email at: dhurghamr.hasan@uokufa.edu.iq.



Ali Al-Ghanimi received his Ph.D. degree from Swinburne University of Technology, Australia. He is currently assistant professor in the Department of Electrical Engineering, Faculty of Engineering, University of Kufa, Iraq. His research interests include robust control, sliding mode control, soft actuators, UAV and intelligent control systems. He has published several papers in international journals and conferences on advanced control techniques for mechatronic systems. He can be contacted at email: alih.alghanimi@uokufa.edu.iq.



Ibrahim H. Al-Kharsan received his B.Sc. degree in electrical engineering from Al-Kufa University, Najaf, Iraq, in 2008, his M.Sc. degree in Electrical and Electronics Engineering from Jawaharlal Nehru Technological University, Hyderabad, India, in 2013, and his Ph.D. degree in Electrical Engineering from the University of Basrah, Iraq, in 2020. His research interests include electrical power engineering, energy management and optimization, and smart grids, with emphasis on intelligent control strategies that integrate renewable energy sources and improve demand-side management. He can be contacted at email: ibrahim.alkharsan@uomus.edu.iq.